The Journal of Navigation (2023), **76**:1 38–61
doi:10.1017/S0373463322000455

RESEARCH ARTICLE

A practical environment potential field modelling method for complex geometric objects

Zhongxian Zhu,[1] Hongguang Lyu,[2]* Jundong Zhang,[1] Yong Yin,[2] and Xiang Fan[3]

[1] Marine Engineering College, Dalian Maritime University, Dalian, China
[2] Navigation College, Dalian Maritime University, Dalian, China
[3] Shanghai Merchant Ship Design and Research Institute, Shanghai, China.
*Corresponding author. E-mail: lhg@dlmu.edu.cn.

Received: 11 November 2021; **Accepted:** 23 July 2022; **First published online:** 15 September 2022

Keywords: unmanned surface vehicle; autonomous; ship collision; trajectory planning; environment potential field modelling; artificial potential field; collision avoidance; maritime autonomous surface ships

Abstract

Several studies have been conducted on collision avoidance (CA) and path planning for maritime autonomous surface ships (MASS) based on artificial potential field (APF) and electronic navigation chart (ENC) data. However, to date, accurate, highly efficient, and automatic modelling of complicated geometry environment potential fields (EPFs) has not been realised. In this study, an accurate EPF model is established using ENC data to describe different types of obstacles, navigable areas, and non-navigable areas. The implicit equations of complex polygons are constructed based on the *R*-function theory, and the discrete-convex hull method is introduced to realise the automatic modelling of EPF. Moreover, collaborative CA and obstacle avoidance (OA) experiments are designed and conducted in a simulated environment and based on the ENC data. The results show that the proposed EPF modelling method is accurate, reliable, and time-efficient even with numerous ENC data and complex shapes owing to the *R*-function representation for geometric objects and discrete-convex hull method. The combination of improved APF and EPF models is proven to be effective for CA and OA. This paper presents a practical EPF modelling approach for APF-based ship path planning.

1. Introduction

1.1. Background

Measures for automatic collision avoidance (CA) and obstacle avoidance (OA) of maritime autonomous surface ships (MASS) are highly complex and uncertain. When considering the motion of the ship, the International Regulations for Preventing Collisions at Sea (COLREGS) and restricted water areas, the automatic CA, OA, and path planning in complex waters are the focus and challenge of recent research works (Lyu and Yin, 2019b; Huang et al., 2020).

The Electronic Chart Display Information System (ECDIS) is an important aid for navigation that must be installed in an up-to-date bridge system. It can present numerous accurate environmental data sets for MASS path planning systems, such as depth of water, obstacles, land areas, and limit of fairways. Therefore, the ideal environment model for a MASS automatic CA system should adapt to the data structure of the electronic navigational chart (ENC) as much as possible (Lyu and Yin, 2019a).

The spatial vector data in accordance with the S-57 and S-101 standards in ECDIS are represented by points, lines (curves), and faces (surfaces). The shapes of objects provided by ECDIS are usually overly complicated and have different characteristic attributes. When vessels navigate in restricted waters

automatically, it is necessary to consider fully the various ENC data and their attributes, establish a navigation environment model, and perform automatic CA and path planning. In this study, establishing the navigational environment model based on the points, lines, and faces of ENC data is a research priority.

1.2. Literature review

1.2.1. Path planning method

Many algorithms have been used and adapted for collision-free path planning, and the techniques and key points of CA have been summarised in literature reviews (Tam et al., 2009; Huang et al., 2020; Panda et al., 2020; Vagale et al., 2021a, 2021b; Zhang et al., 2021; Öztürk et al., 2022). Vagale et al. (2021a) adopted a general categorisation of path planning algorithms based on Souissi et al. (2013), and suggested that such algorithms can be classified as classical approach, advanced approach, and hybrid approach.

The classical approach is a two-step process consisting of (1) environment modelling to prepare for the search and (2) performing the search for the optimal path in this environment. This type of algorithm is used for global path planning where there is no need for local CA. The advanced approach does not require environmental modelling beforehand and can be used to deal with dynamic obstacles, local CA, and path re-planning in real time. The most often used machine learning algorithms (Cheng and Zhang, 2018), potential field methods, velocity obstacles (Kuwata et al., 2014; Chen et al., 2018; Shaobo et al., 2020; Yuan et al., 2021), dynamics widows (Eriksen et al., 2018; Wang et al., 2018), and the vector field histogram method (Tam et al., 2009) can be categorised as this type of approach. The hybrid approach combines several path planning algorithms to ensure safe and feasible navigation both locally and globally. Vagale categorised potential field methods as an advanced approach, according to Serigstad et al. (2018), and indicated that the potential field methods are most often used in path planning owing to their low computational load requirement for trajectory generation, and the trajectory can be generated effectively in real time. However, the disadvantage is the risk of being trapped in local minima (Shi et al., 2007). In addition, expert-based methods are widely used in manned ship supporting system and fuzzy methods (Fiskin et al., 2020; Brcko et al., 2021) are popular for this type of study (Huang et al., 2020).

1.2.2. Artificial potential field-based path planning

In recent years, a series of artificial potential field (APF)-based CA approaches for MASS have been proposed (Chiang et al., 2015; Huang et al., 2020). The APF-based approach established a virtual potential field around the MASS navigation area. The attraction between MASS and the goal, repulsions between MASS and obstacles, and repulsions between MASS and other ships have been comprehensively studied. As the APF controller is easy to construct, intuitive, and effective for handling static and dynamic constraints, it is becoming a key path planning method (Liu and Bucknall, 2015).

Despite being widely applied in research on robot path planning and CA, the APF-based approach faces major technological problems when considering the complicated CA conditions of MASS (Chiang et al., 2015; Huang et al., 2020). Presently, the research priorities of APF-based CA approach are optimising the traditional APF method, solving the 'goals non-reachable with obstacles nearby' (GNRON) problem and local minima problem (Xue et al., 2011; Lyu and Yin, 2018a, 2019b; Fan et al., 2020), cooperative CA and OA through modelling of the environmental potential field (Xue et al., 2011; Pêtrès et al., 2012; Peng et al., 2016; Liu and Bucknall, 2018; Mousazadeh et al., 2018; Wang et al., 2019), and research on the CA problems based on COLREGS (Lyu and Yin, 2018a, 2018b, 2019b). Some researchers have proposed the hybrid path planning methods based on APF and A* methods (Sang et al., 2021) or deep reinforcement learning (Cheng-Bo et al., 2019; Li et al., 2021).

Vagale et al. (2021b) indicated that the COLREGS-constrained APF approach (Lyu and Yin, 2019b) is a fast, effective, and deterministic method for path planning in complex situations with multiple moving target ships and stationary obstacles. This method can account for the unpredictable strategies

https://doi.org/10.1017/S0373463322000455 Published online by Cambridge University Press

of other ships. A hybrid path-guided APF algorithm (Lyu and Yin, 2018a) can provide fast feedback in a changeable environment, and has the potential to rapidly generate adaptive, collision-free, and COLREGS-constrained trajectories in restricted waters and perform path planning on an electronic chart platform (Vagale et al., 2021b). Accordingly, the APF-based approach has been widely applied in the intelligent ship CA systems in open and restricted waters.

1.2.3. Environment potential fields modelling

Currently, related research on environment potential fields (EPF) modelling is based on very simple environment data, and the use of the mass assumption and/or simplification in modelling, and distort the navigable areas or the scope of obstacles. Despite the advantages of APFs, their use is limited by their inability to handle arbitrarily shaped obstacles (Ren et al., 2007). Researches on CA and path planning have rarely been based on the official ENC data, and the complicated geometry EPF modelling problems have not been well resolved. Cooperative CA and OA based on ENC data is still a technical challenge, and related researches cannot satisfy the demands of engineering applications.

Lyu and Yin (2018a, 2019b) systematically studied the multi-ship intelligent CA approach using an improved APF method and considered the rules of COLREGS, manoeuvrability of ship, and uncoordinated CA actions of target ships (TS). They presented a method for EPF map construction based on point, line, and face vector data and their corresponding characteristic attributes provided by electronic charts, and conducted CA tests including dynamic ships and static obstacles in restricted waters. However, the concave line segments were replaced with implicit curves in the EPF modelling of the lines, and obstacles were obtained manually from ECDIS in their work. The complicated concave polygon was split into a series of convex polygons, then all the split polygons were reassembled to establish the potential field of the polygon (Lyu and Yin, 2018a, 2019b). Therefore, their work did not solve the automatic modelling of complicated line and face objects and has an extremely low efficiency.

For arbitrarily shaped face obstacles provided by ENC data, replacing a large amount of concave line segments with curves is inefficient, and obtaining the implicit equations of curves is impractical. Manual splitting of concave polygons will induce different results when using different splitting rules, and may cause distortion or holes in the EPF.

Some researchers use circles (mass point) (Xue et al., 2011; Montiel et al., 2015; Lyu and Yin, 2018b) or convex hull to represent a known polygon (Ren et al., 2007), which may enlarge the action range of the polygon, resulting in losing part of navigation area if the inside of the polygon is unnavigable or navigational hazards if the inside of polygon is navigable (Lyu and Yin, 2018a).

To solve the awkward EPF modelling problems, the *R*-function theory was introduced (Dobkin et al., 1993; Fougerolle et al., 2005; Tao and Tan, 2018) into EPF modelling, and the automatic EPF modelling of face obstacles was realised using the discrete-convex hull method. Accordingly, many experiments have been conducted on APF-based CA projects.

The theory of *R*-functions was first proposed by the former Soviet Union scholar Rvachev in the 1960s and provides an algorithmic method for constructing functions that exactly represent any geometric shape in engineering. The *R*-function is a series of real functions whose result is positive or negative only determined solely by the signs (positive or negative) of the variables, regardless of their values (Rvachev, 1982). In this way, if the implicit representation of the parts is known, any shape that is represented by set theory can be transformed into an implicit inequality by *R*-functions (Varvak, 2015; Gan et al., 2021). Owing to their mathematical properties and natural ability to express complex geometric objects, *R*-functions have been widely used in computer graphics and geometric modelling (Varvak, 2015; Lu and Wang, 2019; Gan et al., 2021; Sukumar and Srivastava, 2022).

1.2.4. Collision risk assessment

Collision risk assessment (CRA) is an important preventive factor in CA at sea and may include several safety criteria based on the current and predicted situations, own or target ship parameters, and their relationships (Vagale et al., 2021b). The most popular method in practice is to utilise two indices to measure the risk, namely distance to closest point of approach (DCPA) and time to closest point of

https://doi.org/10.1017/S0373463322000455 Published online by Cambridge University Press

approach (TCPA) (Huang et al., 2020; Du et al., 2021; Vagale et al., 2021b). The CRA parameters are not limited to DCPA and TCPA, although they are the most commonly used ones. Considering the various navigational factors which were determined as a result of expert interviews, many types of ship domains have been developed for both restricted and open waters (Fiskin et al., 2020; Du et al., 2021; Rawson and Brito, 2021). As an important research branch, the ship domain is crucial for CRA, especially in high-density traffic (Fiskin et al., 2020).

1.3. Motivation

The modelling of the EPF for point and line objects provided by electronic charts is relatively simple (Ren et al., 2007; Xue et al., 2011; Lyu and Yin, 2018a, 2019a). The face objects provided by electronic charts are very high in proportion, such as islands, isobath regions, anchorages, prohibited areas, etc., and their concave and convex shapes are quite complicated (Ren et al., 2007; Lyu and Yin, 2018a). However, the potential field of the face objects cannot be efficiently and accurately constructed by simple 'concave lines' or implicit curves. Therefore, it is necessary to propose a practical method using rigorous mathematical analysis to address the potential field modelling for complicated face objects (Tao and Tan, 2018). The *R*-function theory can be applied to solve the implicit function construction and potential field modelling problems of a complicated geometry (Liu and Ahang, 2001; Wu et al., 2003; Ren et al., 2007).

The motivation of this study is to build an EPF model of the point, line, and face objects provided by the electronic chart; research on the implicit function representation of the complicated polygon based on *R*-functions; solve the automatic EPF modelling problems and realise the cooperative CA and OA of MASS based on the improved APF method.

The remainder of this paper is organised as follows: Section 2 proposes the EPF modelling method based on ENC data. Section 3 illustrates the *R*-function representation for face objects, and describes the EPF modelling procedure for complex face objects. Section 4 describes the path planning method based on the improved APF. Collaborative CA and OA experiments are presented in Section 5. The discussion and conclusions are presented in Sections 6 and 7, respectively.

2. EPF Modelling for objects provided by ENC

Because the spatial vector data in accordance with the S-57 and S-101 standards are represented by points, lines (curves), and faces (surfaces), through inquiring on the attributes of each object, the type and degree of danger of any object can be defined. The corresponding safe distances can be selected to ensure that the MASS can safely pass through.

2.1. EPF modelling for point objects

If there are N point objects in the two-dimensional (2D) plane and an i-th ($i = 1, 2, \cdots, N$) object with position $p_i(x_i, y_i)$, the distance between any position $p(x, y)$ and p_i is $f_{\text{Point}-i} = \sqrt{(x - x_{\text{i}})^2 + (y - y_{\text{i}})^2}$, and the potential field at location $p(x, y)$ can be written as:

$$f_{\mathbf{Point}}(\boldsymbol{p}) = \sum_{\boldsymbol{i}=\mathbf{1}}^{N} \frac{\mathbf{1}}{\mathbf{1}+\mathbf{e}^{\boldsymbol{\beta}_i f_{\mathbf{Point}-\boldsymbol{i}}}} \tag{1}$$

where $\boldsymbol{\beta_i}$ is the i-th positive parameter of the point object; the larger the value of $\boldsymbol{\beta_i}$, the steeper the potential field and the smaller the action range. Otherwise, the smaller the value of $\boldsymbol{\beta_i}$, the flatter the potential field and the larger the action range. Figure 1 shows the different action ranges and potential surfaces for different $\boldsymbol{\beta_i}$. The potential field reaches the maximum value of $1 \cdot 0$ at position $p_i(x_i, y_i)$ and approaches $0 \cdot 0$ at positions far away from $p_i(x_i, y_i)$.

https://doi.org/10.1017/S0373463322000455 Published online by Cambridge University Press

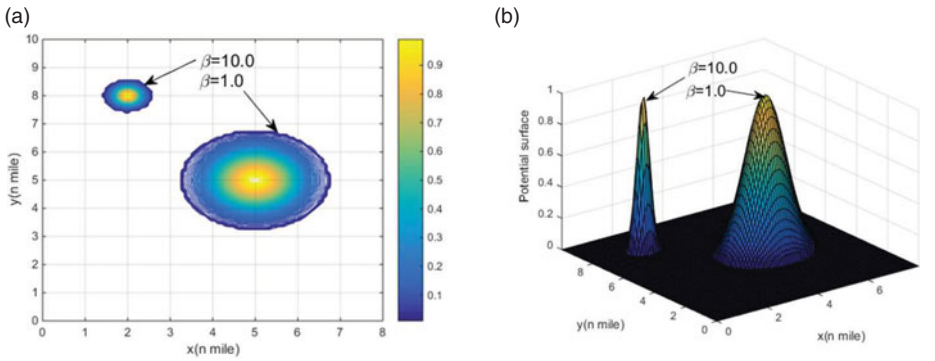

Figure 1. *Potential field for point objects with different values of* $\boldsymbol{\beta_i}$*: (a) potential contours, (b) potential surfaces.*

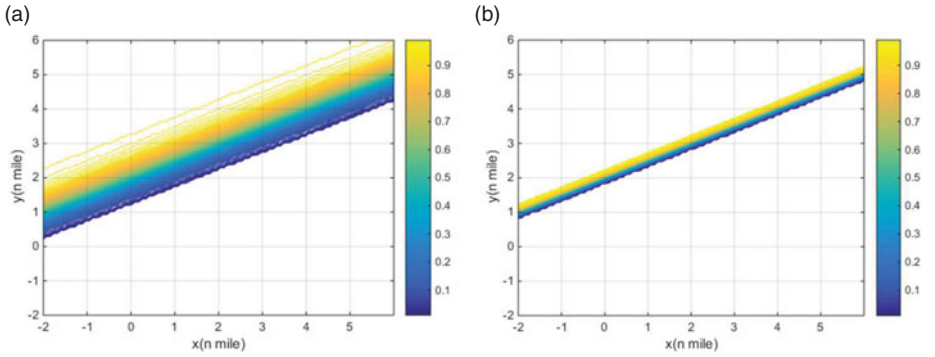

Figure 2. *Potential fields for line objects: (a)* $\boldsymbol{\gamma_i} = 1.0$*, (b)* $\boldsymbol{\gamma_i} = 5.0$*.*

2.2. EPF modelling for line objects

Line objects provided by the electronic chart are represented by a group of line segments. Among the anticlockwise sorted line segments, if the i-th line segment $p_i\vec{p}_{i+1}$ starts from $p_i(x_i, y_i)$ and ends at $p_{i+1}(x_{i+1}, y_{i+1})$, then the implicit function of the line segment is $f_{\text{Line - }i} = A_i x + B_i y + C_i$. For any point $p(x, y)$, it is on the line when $f_{\text{Line - }i} = 0$, or on the left side of the line when $f_{\text{Line - }i} > 0$, or on the right side of the line when $f_{\text{Line - }i} < 0$. The potential field of the line object can be expressed as:

$$f_{\text{Line}}(\boldsymbol{p}) = \sum_{i=1}^{N} \frac{1}{1+\mathrm{e}^{-\gamma_i f_{\text{Line-}i}}} \tag{2}$$

where $\boldsymbol{\gamma_i}$ is the i-th positive parameter of the line segment that determines the influence range of the line; the smaller the value of $\boldsymbol{\gamma_i}$ means the flatter the potential field and the larger the action range of the line; otherwise, a larger value of $\boldsymbol{\gamma_i}$ means a steeper potential field and a smaller action range of the line. As shown in Figure 2, when $f_{\text{Line - }i} = 0$, the point $p(x, y)$ is on the line segment, and the potential field value is $0 \cdot 5$. If $f_{\text{Line - }i} > 0$, the potential field value is larger, and the maximum is $1 \cdot 0$. If $f_{\text{Line - }i} < 0$, the potential field value is smaller, and the minimum value is 0.

2.3. EPF modelling for face objects

If there are N face objects in the 2D plane, then each face object is represented by a group of anticlockwise sorted line segments. If we can obtain the mathematical expression $F_i(x, y)$ of the face object and let the

https://doi.org/10.1017/S0373463322000455 Published online by Cambridge University Press

Table 1. *Recommended $\boldsymbol{\beta}$, $\boldsymbol{\gamma}$, and $\boldsymbol{\alpha}$ values for different objects.*

Object	Features	Safe distance (nm)	Parameter
point	wrecks, reefs	$1 \cdot 716$	$\boldsymbol{\beta} = 1 \cdot 0$
	aids to navigation	$0 \cdot 543$	$\boldsymbol{\beta} = 10 \cdot 0$
line	safety contours	$2 \cdot 634$	$\boldsymbol{\gamma} = 0 \cdot 10$
	channel limits	$0 \cdot 132$	$\boldsymbol{\gamma} = 2 \cdot 0$
face	islands, shoals	$>3 \cdot 0$	$\boldsymbol{\alpha} < 1 \cdot 0$
	closed isobaths	$0 \cdot 1$	$\boldsymbol{\alpha} = 50 \cdot 0$

points inside the polygon fulfil the expression $F_i(x, y) < 0$, let points on the edge fulfil the expression $F_i(x, y) = 0$, and let points outside the polygon fulfil the expression $F_i(x, y) > 0$, then the potential field of face object can be expressed as:

$$\boldsymbol{f}_{\mathbf{face}}(\boldsymbol{p}) = \sum_{\boldsymbol{i}=\mathbf{1}}^{\boldsymbol{N}} \frac{\mathbf{1}}{\mathbf{1}+\mathbf{e}^{-\boldsymbol{\alpha}_{\boldsymbol{i}}\boldsymbol{F}_{\boldsymbol{i}}(\boldsymbol{x},\boldsymbol{y})}} \tag{3}$$

where $\boldsymbol{\alpha_i}$ is the positive parameter of the i-th face object. Similarly, the smaller the value of $\boldsymbol{\alpha_i}$, the flatter the potential field and the larger the action range of the face object. Otherwise, the larger the value of $\boldsymbol{\alpha_i}$, the steeper the potential field and the smaller the action range of the face. If $F_i(x, y) = 0$, point $p(x, y)$ is on the edge of the face object, and the potential field value is $0 \cdot 5$. If $F_i(x, y) > 0$, $p(x, y)$ is outside the face object, then the potential field value is smaller, and the minimum is 0. If $F_i(x, y) < 0$, $p(x, y)$ is inside the face object, the potential field value is larger, and the maximum is $1 \cdot 0$.

A MASS should maintain a safe distance from islands or shallow waters when navigating. However, sometimes it is required to navigate inside certain navigable regions and maintain a safe distance from the edges of the region, such as navigating in channels, traffic separation schemes, or other safe navigable areas. The potential field of the face object can be expressed as:

$$\boldsymbol{f}_{\mathbf{face}\text{-}\boldsymbol{i}} = \mathbf{1} - \frac{\mathbf{1}}{\mathbf{1}+\mathbf{e}^{-\boldsymbol{\alpha}_{\boldsymbol{i}}\boldsymbol{F}_{\boldsymbol{i}}(\boldsymbol{x},\boldsymbol{y})}} \tag{4}$$

where the inside of the face is navigable, the potential field is smaller, and the minimum is 0; whereas the outside of the face is unnavigable, and the potential field approaches $1 \cdot 0$ if it is far away from the face object.

2.4. EPF of the entire static environment

If there are M, N, and Q point objects, line objects, and face objects around the MASS, respectively, then the total potential field of the entire static environment can be obtained by adding the potential field generated by the point objects, line objects, and face objects. The environmental potential field at $p(x, y)$ can then be expressed as:

$$\boldsymbol{f}(\boldsymbol{p}) = \boldsymbol{f}_{\mathbf{face}}(\boldsymbol{p}) + \boldsymbol{f}_{\mathbf{Line}}(\boldsymbol{p}) + \boldsymbol{f}_{\mathbf{Point}}(\boldsymbol{p}) \tag{5}$$

Each spatial object has a unique attribute for navigation. By setting the appropriate values for $\boldsymbol{\beta}$, $\boldsymbol{\gamma}$, and $\boldsymbol{\alpha}$ to specify the action ranges of the object, the recommended parameter for each spatial object and the safe distance to be maintained are listed in Table 1.

https://doi.org/10.1017/S0373463322000455 Published online by Cambridge University Press

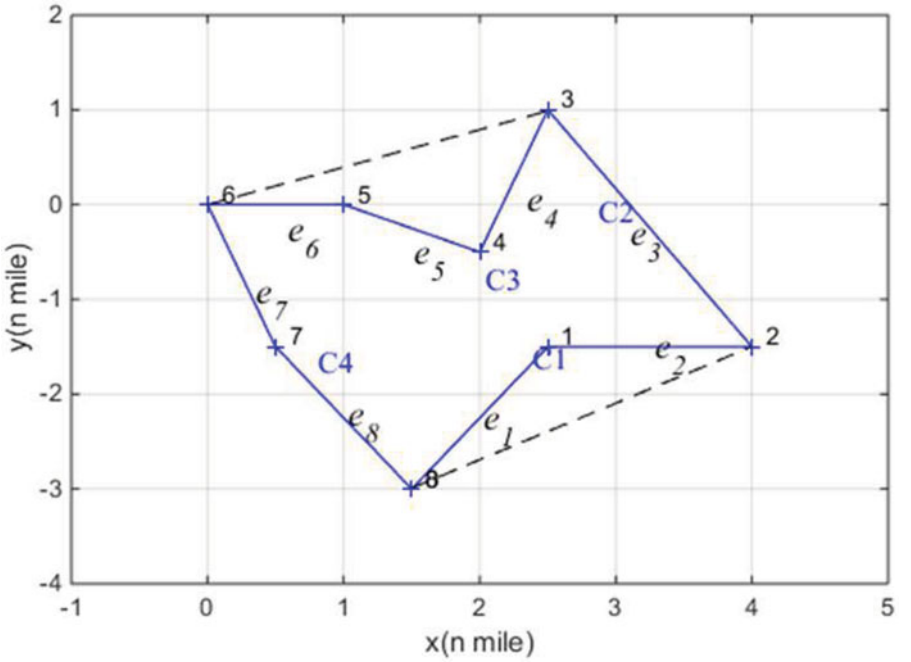

Figure 3. *Convex hull and side-chains of polygon* ***B****.*

3. *R*-function representation for geometric object

3.1. Theory of R-function

For the geometry in the 2D plane (as shown in Figure 3), the equation for each edge can be expressed by an implicit function $f_i(x, y) = 0$. The implicit function separates the plane into two half-spaces. The points on the line fulfil the expression of $f_i(x, y) = 0$, and the points in the half-space fulfil the expression of $f_i(x, y) > 0$ or $f_i(x, y) < 0$. For an arbitrary closed shape, if the vertices are sorted anticlockwise, the inner part of the shape can be expressed by the left half-space of each edge ($f_i(x, y) < 0$). Therefore, the *R*-function can be used to express the region enclosed by two inequalities as function operations; through algebra operations to the implicit function of each edge, we can obtain the expressions $F(x, y) < 0$, $F(x, y) = 0$, and $F(x, y) > 0$ to express that point $p(x, y)$ is internal, boundary, or external to the geometric object.

The *R*-function is a real-value function characterised by a property that is completely determined by the sign of its arguments rather than its value. Rvachev presented a series of useful *R*-functions with sufficient completeness, where R_a is an *R*-function system:

$$R_a = \frac{1}{1+a}(x + y \pm \sqrt{x^2 + y^2 - 2axy}) \tag{6}$$

where $a = a(x, y)$ is an arbitrary continuous and symmetric function and fulfilled by the expression $-1 < a(x, y) \leq 1$. The symbol $\pm$ denotes the *R*-conjunction and *R*-disjunction. If $a = 0$ or $a = 1$, the widely used R_0 system and R_1 system are as follows:

$$R_0 = x + y \pm \sqrt{x^2 + y^2} \tag{7}$$

$$R_1 = x + y \pm |x - y| \tag{8}$$

Compared with other *R*-function systems, the R_0 system is differentiable except at the origin, and the calculation is simple. In this study, we select the R_0 system to represent the geometric objects.

https://doi.org/10.1017/S0373463322000455 Published online by Cambridge University Press

The implicit function based on the aforementioned approach cannot accurately calculate the signed distance between a space point and an object boundary, so normalised function was introduced into the geometric object expression. For line segments expressed as $f_{\text{Line - }i} = A_i x + B_i y + C_i$, its normalised function is:

$$f_{\text{Line - }i} = \frac{A_i}{Q}x + \frac{B_i}{Q}y + \frac{C_i}{Q}, \quad Q = \sqrt{{A_i}^2 + {B_i}^2} \tag{9}$$

3.2. R-function representation for geometric objects

Arbitrary geometric objects can be expressed by several basic primitives through regular Boolean operations ('intersection' or 'union'). The geometric object $\boldsymbol{B}$ can be expressed in the following form:

$$B = F[B_1, B_2, \cdots, B_n] \tag{10}$$

where $B_i (i = 1, 2, \cdots, n)$ is a basic primitive and F is a regular Boolean function with operations of $\cap^*$, $\cup^*$, and $-^*$. If the logical operations $\wedge$, $\vee$, and $\neg$ are used to displace the Boolean operations, then F becomes a logical function. Combined with the definition of the R-function, the geometric object B can be expressed as follows:

$$F[S(B_1), S(B_2), \cdots, S(B_n)] = 1 \tag{11}$$

where the basic primitive B_i is the half-space of the geometric object expressed by an implicit function $f_i(x) \leq 0$. If the signed distance function $f_i(x)$ for basic primitive B_i is:

$$B_i : f_i(x) \geq 0 \quad (i = 1, 2, \cdots, n) \tag{12}$$

then Equation (10) can be written as:

$$F[S(f_1), S(f_2), \cdots, S(f_n)] = 1 \tag{13}$$

According to Equation (13), given a continuous function $f(x)$ and its correlation function $F(X_1, X_2, \cdots, X_n)$, the geometric object $\boldsymbol{B}$ can be expressed as:

$$f(f_1, f_2, \cdots, f_n) \geq 0 \tag{14}$$

where $f_i (i = 1, 2, \cdots, n)$ is a real continuous function, and f is the implicit function of $\boldsymbol{B}$. Because the geometric objects in this study are all in the 2D plane and without any curves or surfaces, the implicit function of the geometric object is accurate for expressing the object. Otherwise, the implicit function approximately expresses the geometric object.

3.3. Discrete-convex hull method

The expression of the geometric object using R-function is a semi-analytical solution based on its constructive solid geometry(CSG) model, and the implicit function can be used to accurately express the geometric object in the 2D plane. CSG representations usually have various logical and implicit functions, but they have the same logical functionality. In fact, the automatic generation of a CSG representation for an overly complex object is an intractable task. However, existing algorithms can automatically generate the CSG representations for polygonal regions. A polygonal region can be automatically divided into side-chains with the intersection of convex hull vertices. The intersection of the half-space defined by side-chains can then be adopted to express a polygonal region, whereas the half-space is represented by the intersection or union of the edges. If the intersection of the two edges is concave, the half-space is the union; otherwise, it is the intersection. The region $\boldsymbol{B}$ shown in Figure 3

https://doi.org/10.1017/S0373463322000455 Published online by Cambridge University Press

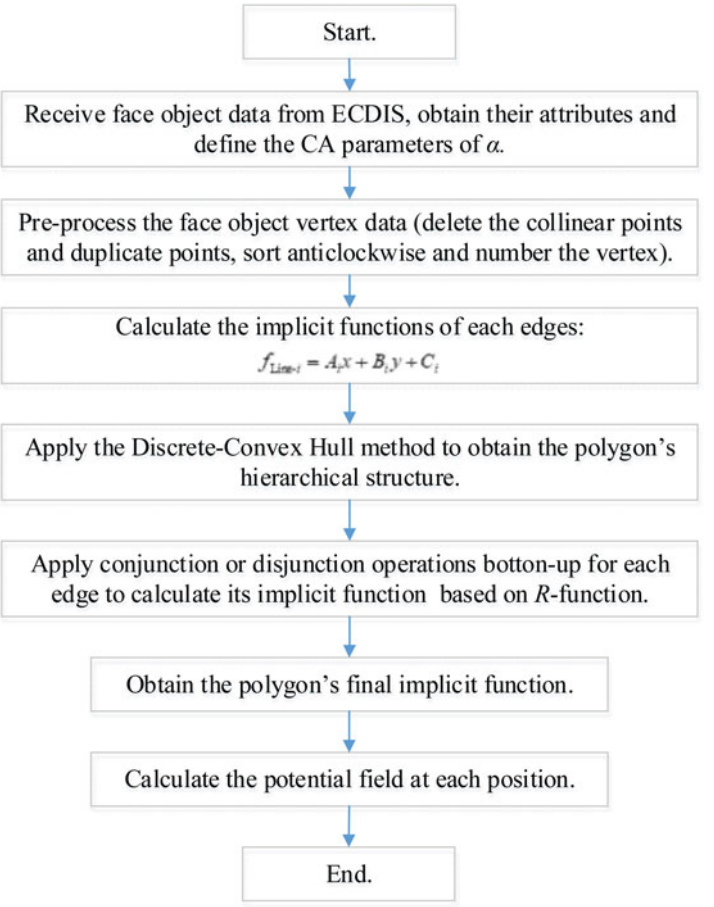

Figure 4. *EPF modelling procedure for complex face object.*

has the logical function $B = C_1 \wedge C_2 \wedge C_3 \wedge C_4$. Here, $C_1 = e_1 \vee e_2$,$C_2 = e_3$,$C_3 = e_4 \vee (e_5 \wedge e_6)$ and $C_4 = e_7 \wedge e_8$.

The aforementioned approach for dealing with a geometric object is referred to as the discrete-convex hull method. As mentioned previously, the face objects in this study are represented by a group of anticlockwise sorted line segments in the 2D plane; their implicit functions are accurate for expressing geometric objects. Therefore, the implicit function of a geometric object has a value of 0 at the boundary of the object, and the internal and external points have values <0 and >0, respectively.

3.4. EPF modelling procedure for complex face object

The procedure of EPF modelling for complex face objects can be summarised as follows (as shown in Figure 4). First, data on the face objects are received from ECDIS, the attributes are obtained, and the CA parameters of α are defined to specify their action ranges. Second, the vertices of the face objects are pre-processed, including deleting collinear or duplicate points, sorting anticlockwise, and numbering. Third, the implicit functions of each edge were calculated, and the discrete-convex hull method is applied to obtain the hierarchical structure of the polygon. Fourth, the conjunction or disjunction operation is applied bottom-up for each edge to obtain an implicit function based on the *R*-function. Finally, the implicit function of the polygon is obtained, and the potential field at each position is calculated.

https://doi.org/10.1017/S0373463322000455 Published online by Cambridge University Press

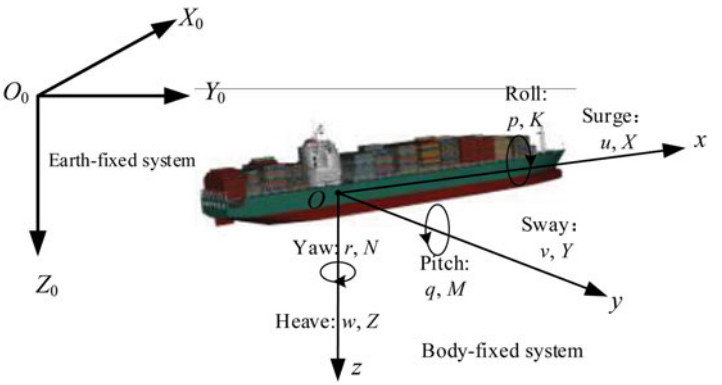

Figure 5. *Coordinate system of ship motion.*

4. Path planning

CA and path planning for MASS is a complex system that is constrained by COLREGS and should cope with static and dynamic environments in real time. Following the work of Lyu and Yin (2019b, 2018b), we used a path-guided hybrid APF method (PGHAPF) to realise MASS CA and OA.

4.1. Modelling of motions of MASS

To describe the motion of a MASS in CA, the Earth- and body-fixed coordinate systems were constructed as shown in Figure 5. The vector $\boldsymbol{\eta} = [x, y, z, \phi, \theta, \psi]^{\mathrm{T}}$ represents the position and altitude of MASS in the Earth-fixed system, and the vector $\boldsymbol{\nu} = [u, v, w, p, q, r]^{\mathrm{T}}$ represents the speed and rotation speed in the body-fixed system. The 6-DOF mathematical model of the MASS can be expressed as:

$$\begin{cases} (m+m_x)\dot{u} - (m+m_y)vr + (m+m_z)wq = X_H + X_G + X_P + X_R + X_{\mathrm{Env}} \\ (m+m_y)\dot{v} + (m+m_x)ur - (m+m_z)wp = Y_H + Y_G + Y_P + Y_R + Y_{\mathrm{Env}} \\ (m+m_z)\dot{w} - (m+m_x)uq + (m+m_y)vp = Z_H + Z_G + Z_P + Z_R + Z_{\mathrm{Env}} \\ (I_{xx}+J_{xx})\dot{p} + (I_{zz}+J_{zz}-I_{yy}-J_{yy})qr + (m_z-m_y)vw = K_H + K_G + K_P + K_R + K_{\mathrm{Env}} \\ (I_{yy}+J_{yy})\dot{q} + (I_{xx}+J_{xx}-I_{zz}-J_{zz})pr + (m_x-m_z)uw = M_H + M_G + M_P + M_R + M_{\mathrm{Env}} \\ (I_{zz}+J_{zz})\dot{r} + (I_{yy}+J_{yy}-I_{xx}-J_{xx})pq + (m_y-m_x)uv = N_H + N_G + N_P + N_R + N_{\mathrm{Env}} \end{cases} \tag{15}$$

where $m = \rho_s \nabla$ represents the mass of the vessel; ρ_s is the seawater density; ∇ is the displacement; m_x, m_y, and m_z denotes the mass added to the vessel; I_{xx}, I_{yy}, I_{zz}, J_{xx}, J_{yy}, J_{zz} denote the moments and added moments of inertia; the subscripts H and G represent the viscous hydrodynamics and hydrostatic forces exerted on the naked hull; the subscripts P and R are the forces and moments generated by the propeller and rudder; the subscript 'Env' denotes the external disturbance forces induced by wind, wave, and current.

4.2. Modified APF model

The attractive F_{att} and repulsive F_{rep} forces exerted on the ship under varying conditions were established by referring to the work of Lyu and Yin (2018a, 2019a). Because of the numerous and undefined parameters for CA, the CA results have no direct relationship with the CA parameters, and the cited work of Lyu and Yin is therefore incomprehensible and unacceptable for navigators. As the DCPA-TCPA is the essential criterion rule for 'risk of collision' in navigation, we modified the negotiation CA

https://doi.org/10.1017/S0373463322000455 Published online by Cambridge University Press

repulsive force F_{rd} and emergency CA repulsive force F_{re} as follows:

$$F_{\mathrm{att}} = \varepsilon d_{\mathrm{og}} \overrightarrow{n_{\mathrm{og}}} \tag{16}$$

$$F_{\mathrm{rep}}(p,v) = \begin{cases} F_{\mathrm{rd1}} + F_{\mathrm{rd2}} + F_{\mathrm{rd3}}, & \text{if } d_{\mathrm{emg}} < d \le d_{\mathrm{neg}},\ \theta < \theta_m, 0 \le d_{\mathrm{CPA}} \le d\mathrm{TOL}_{\mathrm{neg\,-\,CPA}}, \\ & \qquad 0 \le t_{\mathrm{CPA}} \le t\mathrm{TOL}_{\mathrm{neg\,-\,CPA}} \\ F_{\mathrm{re1}} + F_{\mathrm{re2}} + F_{\mathrm{re3}}, & \text{if } d \le d_{\mathrm{emg}}, \qquad 0 \le \mathrm{d}_{\mathrm{CPA}} \le d\mathrm{TOL}_{\mathrm{emg\,-\,CPA}}, \\ & \qquad 0 \le t_{\mathrm{CPA}} \le t\mathrm{TOL}_{\mathrm{emg\,-\,CPA}} \\ 0 & \text{otherwise} \end{cases} \tag{17}$$

$$\begin{aligned} \boldsymbol{F}_{\mathrm{rd1}} = & -\eta_d {d_g}^2 \\ & \left[\left(\frac{1}{d - d_{\mathrm{emg}}} - \frac{1}{d_{neg} - d_{\mathrm{emg}}} \right) e^{\theta_m - \theta} \left(\frac{d\mathrm{TOL}_{\mathrm{neg\,-\,CPA}}}{d\sqrt{d^2 - {d_{\mathrm{emg}}}^2}} + \frac{\sin\theta}{||\boldsymbol{v}_{ot}||} \right) + \frac{e^{\theta_m - \theta} - 1}{(d - d_{\mathrm{emg}})^2} \right. \\ & \left. - \left(\frac{1}{d - d_{\mathrm{emg}}} - \frac{1}{d_{neg} - d_{\mathrm{emg}}} \right) \left(\frac{d_{\mathrm{emg}}}{d\sqrt{d^2 - {d_{\mathrm{emg}}}^2}} + \frac{\sin\theta_m}{||\boldsymbol{v}_{ot}||} \right) \right] \boldsymbol{n}_{ot} \end{aligned} \tag{18}$$

$$\begin{aligned} \boldsymbol{F}_{\mathrm{rd2}} = & \pm\eta_d {d_g}^2 \\ & \left[\left(\frac{1}{d - d_{\mathrm{emg}}} - \frac{1}{d_{neg} - d_{\mathrm{emg}}} \right) e^{\theta_m - \theta} \left(\frac{1}{||\boldsymbol{p}_{ot}||} + \frac{\cos\theta}{||\boldsymbol{v}_{ot}||} \right) + \frac{||\boldsymbol{v}_{ot\perp}||(e^{\theta_m - \theta} - 1)}{d(d - d_{\mathrm{emg}})^2} \right. \\ & \left. - \left(\frac{1}{d - d_{\mathrm{emg}}} - \frac{1}{d_{neg} - d_{\mathrm{emg}}} \right) \left(\frac{1}{||\boldsymbol{p}_{ot}||} + \frac{\cos\theta_m}{||\boldsymbol{v}_{ot}||} \right) \right] \boldsymbol{n}_{ot\perp} \end{aligned} \tag{19}$$

$$\boldsymbol{F}_{\mathrm{rd3}} = \eta_d d_g \left(\frac{1}{d - d_{\mathrm{emg}}} - \frac{1}{d_{neg} - d_{\mathrm{emg}}} \right) (e^{\theta_m - \theta} - 1) \boldsymbol{n}_{og} \tag{20}$$

$$\boldsymbol{F}_{\mathrm{re1}} = -2\eta_{\mathrm{e}} {d_g}^2 \left[\left(\frac{1}{d - d\mathrm{TOL}_{\mathrm{emg\,-\,CPA}}} - \frac{1}{d_{\mathrm{emg}}} \right) \times \frac{1}{(d - d\mathrm{TOL}_{\mathrm{emg\,-\,CPA}})^2} + ||\boldsymbol{v}_{ot}|| \cos\theta \right] \boldsymbol{n}_{ot} \tag{21}$$

$$\boldsymbol{F}_{\mathrm{re2}} = 2\eta_{\mathrm{e}} \frac{{d_g}^2}{d} (||\boldsymbol{v}_{ot}||^2 \cos\theta \sin\theta) \boldsymbol{n}_{ot\perp} \tag{22}$$

$$\boldsymbol{F}_{\mathrm{re3}} = 2\eta_{\mathrm{e}} d_g \left[\left(\frac{1}{d - d\mathrm{TOL}_{\mathrm{emg\,-\,CPA}}} - \frac{1}{d_{emg}} \right)^2 + ||\boldsymbol{v}_{ot}||^2 \cos^2\theta \right] \boldsymbol{n}_{og} \tag{23}$$

where the direction and significance of each force are shown in Figure 6. The term $\boldsymbol{n}_{ot}$ denotes a unit vector pointing to TS or obstacle from own ship (OS); d_g is the distance between OS and the goal; d is the distance between OS and TS; θ_{m} is the angle between any tangent line ($\boldsymbol{T_1 p_{os}}$ or $\boldsymbol{T_2 p_{os}}$) and the relative position vector $\boldsymbol{p_{os}} \boldsymbol{p_{ts}}$;$\theta$ is the angle between the relative position vector $\boldsymbol{p}_{\mathrm{ot}}(\boldsymbol{p}_{\mathrm{ot}} = \boldsymbol{p}_{\mathrm{ts}} - \boldsymbol{p}_{\mathrm{os}})$ and the relative speed vector $\boldsymbol{v}_{\mathrm{ot}}(\boldsymbol{v}_{\mathrm{ot}} = \boldsymbol{v}_{\mathrm{os}} - \boldsymbol{v}_{\mathrm{ts}})$. The risk of collision occurs when the extension line of $\boldsymbol{v}_{\mathrm{os}}$ crosses the circle of radius $d\mathrm{TOL}_{\mathrm{neg\,-\,CPA}}(\theta < \theta_{\mathrm{m}})$; otherwise, the OS can pass through the TS with a safe distance larger than $d\mathrm{TOL}_{\mathrm{neg\,-\,CPA}}$. Because the algorithm works on a 2D Cartesian system, we use the Euclidean distance rather than measuring the distance with the haversine formulas.

https://doi.org/10.1017/S0373463322000455 Published online by Cambridge University Press

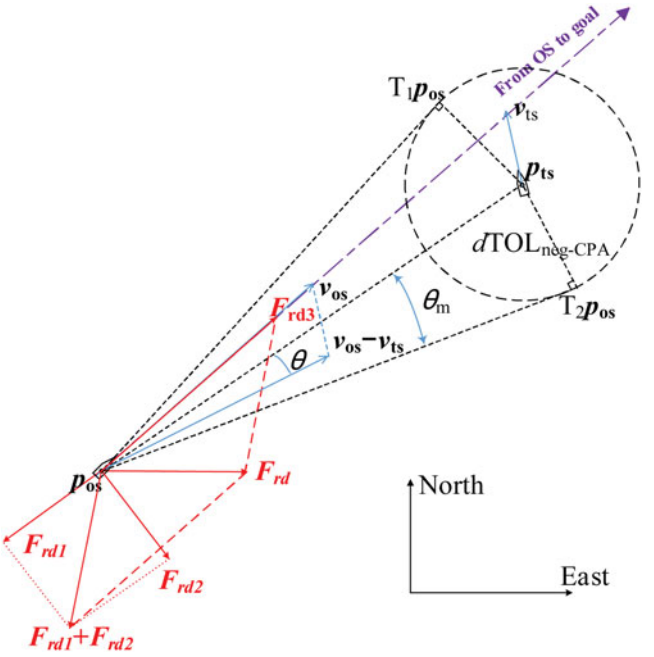

Figure 6. *Repulsive forces for TS.*

Terms d_{emg} and d_{neg} represent the distance criterion of emergency CA and negotiation CA, respectively, $d\text{TOL}_{neg\text{-}CPA}$ and $t\text{TOL}_{neg\text{-}CPA}$ denote the distance and time criteria of negotiation CA, respectively, and $d\text{TOL}_{emg\text{-}CPA}$ and $t\text{TOL}_{emg\text{-}CPA}$ represent the distance and time criteria of emergency CA, respectively. Because all the CA parameters have actual meanings in navigation, and the CA results correspond well to the CA parameters, the modification of the repulsive force model can be comprehended and accepted by navigators.

If there are N TSs, the total repulsive force can be obtained by adding the repulsive forces generated by each TS. The ship will take the corresponding CA actions under the resultant F_{sum} for varying conditions and reach the goal. Based on the calculation of attractive and repulsive forces, the total virtual force exerted on the ship can be obtained as:

$$F_{\text{sum}} = F_{\text{att}} + F_{\text{rep}} \tag{24}$$

5. Tests and results

5.1. EPF modelling for face objects

EPF modelling of convex polygons is uncomplicated because the implicit functions of polygons can be obtained using a one-layer intersection operation (∧). The potential field at any position generated by the polygons can be obtained as shown in Figure 7.

If the polygon includes one or more concave points, the discrete-convex hull method should be applied to obtain its hierarchical structure; the implicit function can then be obtained bottom-up based on the *R*-function theory. There is only one concave point in Figures 8(a) and 8(b), and the implicit functions of the polygons can be obtained using a two-layer discrete-convex hull calculation, whereas the polygon in Figure 8(c) requires a three-layer discrete-convex hull calculation.

Figure 9 shows the potential field with different values of α. It is obvious that a smaller value of α generates a larger action range of the potential field (the navigable area is smaller around the object).

https://doi.org/10.1017/S0373463322000455 Published online by Cambridge University Press

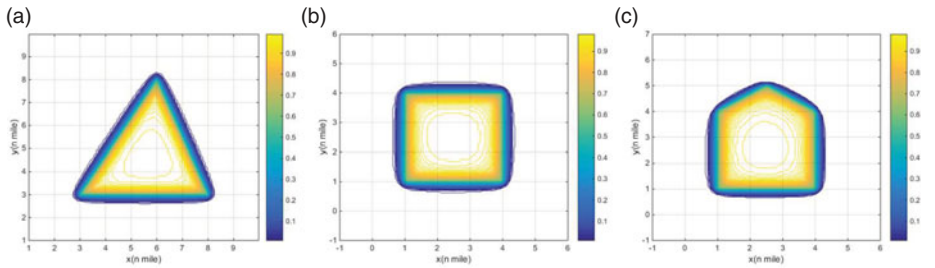

Figure 7. *Potential fields generated by convex polygons ($\alpha = 10 \cdot 0$): (a) triangle, (b) quadrangle, (c) pentagon.*

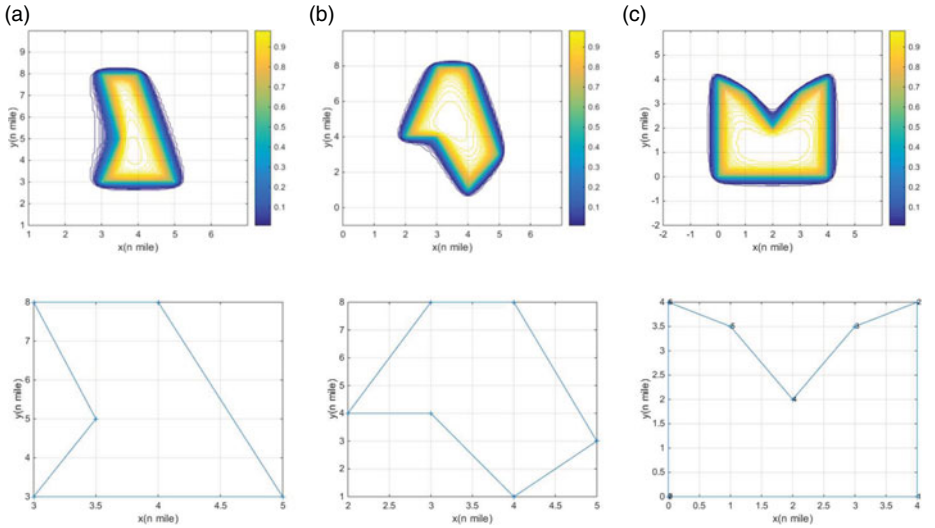

Figure 8. *Potential fields generated by concave polygons ($\alpha = 10 \cdot 0$): (a) pentagon, (b)hexagon, (c) heptagon.*

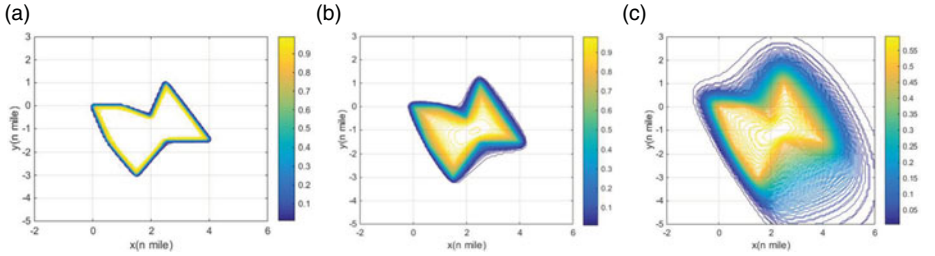

Figure 9. *Potential fields with different α values: (a) $\alpha = 50 \cdot 0$, (b) $\alpha = 10 \cdot 0$, (c) $\alpha = 1 \cdot 0$.*

The approach proposed in this study provides an edge-smoothed potential field. The potential field was well-smoothed even around the sharp vertices, which is beneficial for the OA of the MASS.

For the polygons shown in Figure 10, their hierarchical structures (as shown in Figure 11) are quite difficult to obtain owing to their complex shapes and concave-convex structures. In current research, automatic potential field modelling of these types of polygons is impractical, while the EPF can be effectively obtained in this study.

As shown in Figure 12, the hierarchical structure of the polygon becomes more complex when new vertices inserted, the potential field around the inserted points changes accordingly, and the potential

https://doi.org/10.1017/S0373463322000455 Published online by Cambridge University Press

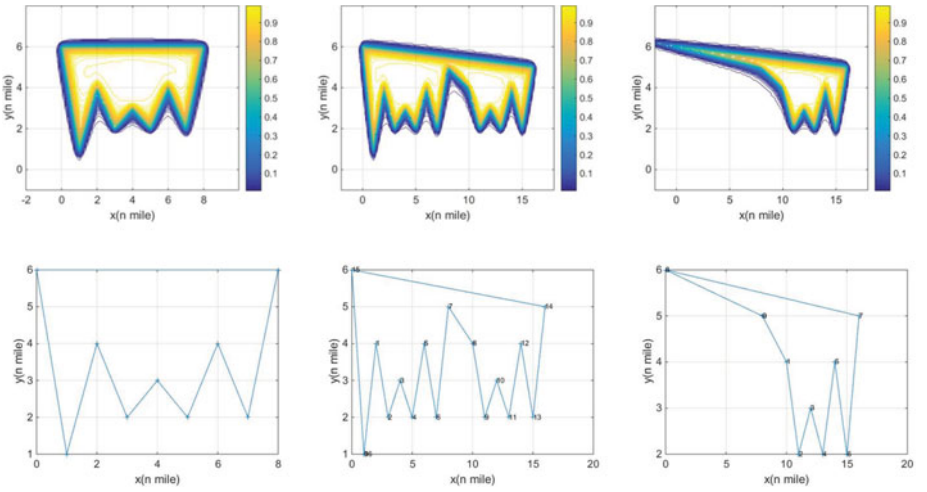

Figure 10. *Potential fields of complex polygons ($\alpha = 10 \cdot 0$).*

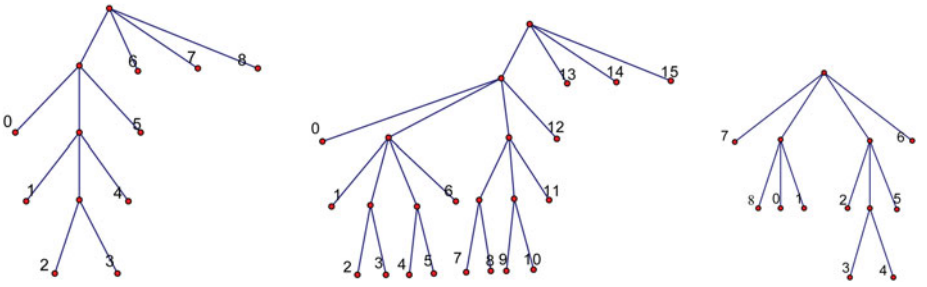

Figure 11. *Hierarchical structure of complex polygons.*

field far away remains unchanged. The approach proposed in this study is proven to be feasible and reliable for solving these complicated potential field modelling problems.

5.2. EPF modelling based on ENC data

In the vector data provided by the shipboard electronic chart, the 20.0 m isobath data around Zhangzidao (Dalian, China) consist of four islands with 511 sampling points (as shown in Figure 13) (chart number = CN311001, issue date = 2015-08-18, update number = 6, update application date = 2017-12-26, scale = 1:90,000, horizontal geodetic datum = WGS 84). To demonstrate the problem-solving capability of the approach proposed in this study, a series of well-designed tests were conducted using a personal computer with an Intel(R) Xeon(R) CPU E5-1600 v3 @ $3 \cdot 5$ GHz processor, 8 GB RAM, and a 64-bit Windows 10 Professional operating system.

The potential field around Zhangzidao Island was generated based on the $20 \cdot 0$ m isobath data. As shown in Figure 14, a larger value of α results in a larger safe navigation region for the ship, whereas a smaller value of α implies that the ship should maintain a larger distance from the islands. Although a considerable amount of data were provided by the electronic chart, and the shapes of the polygons are extremely complicated, the proposed algorithm could successfully realise the environmental potential field modelling.

Figure 15 shows the EPF modelling time of the $20 \cdot 0$ m isobath data. The EPF calculation time for each space point is less than $0 \cdot 1$ ms in each iteration. The calculation was relatively time consuming when numerous ENC data were initially imported, because the discrete-convex hull method was applied to

https://doi.org/10.1017/S0373463322000455 Published online by Cambridge University Press

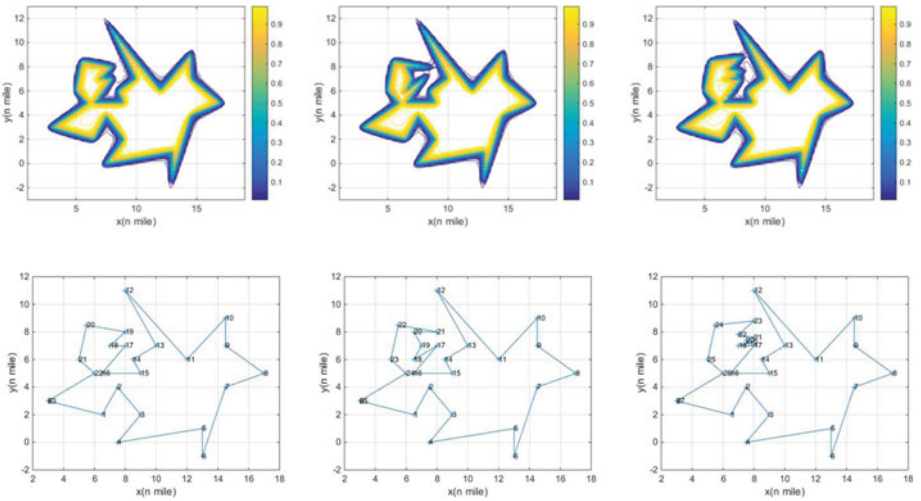

Figure 12. *Potential fields of very complex polygons.*

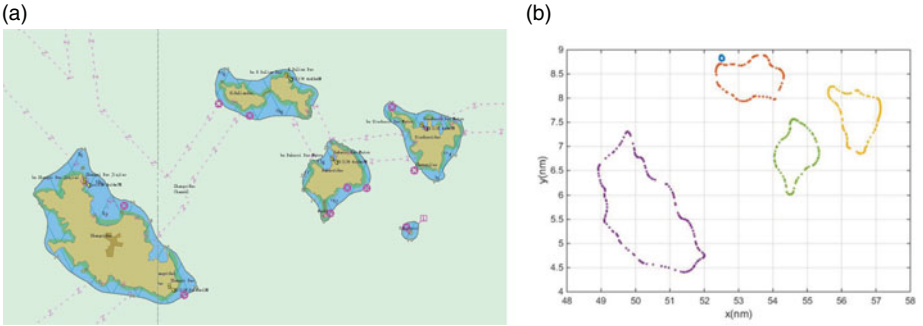

Figure 13. *20 · 0 m isobath and sampling points near Zhangzidao islands: (a) 20 · 0 m isobath, (b) sampling points.*

obtain the hierarchical structures and the implicit functions based on the *R*-function theory. Subsequently, the potential field calculation for each point has no direct relationship with the amount and shape of the ENC data. The approach proposed in this study has very small calculations even when operating numerous space data; thus, it can be used in real-time EPF modelling for MASS.

5.3. Path planning in restricted water

This section presents how one container ship, *KangHe*, was used as OS to test the OA capability based on the aforementioned 20 · 0 m isobath data. The CA parameters and initial conditions of the ship are presented in Table 2. $\alpha = 50 \cdot 0$ was set for the 20 · 0 m isobath data. The ship was designed to navigate across three islands successively in accordance with the route plan, and simultaneously detect and maintain a safe distance from obstacles.

As shown in Figure 16, the OA result shows that *KangHe* can promptly detect the obstacles and accomplish the OA actions. Figures 17 and 18 show the course and speed changing processes during the test. In the first 20 min, *KangHe* detected the risk of collision with the first island and altered its course to starboard with a smaller potential field size than the port side. The speed of the ship decreased owing to the frequent operation of the rudder. At 21 min, *KangHe* headed for the goal with an extra left turn when it had passed the first island, and the speed increased immediately owing to the stable large rudder

https://doi.org/10.1017/S0373463322000455 Published online by Cambridge University Press

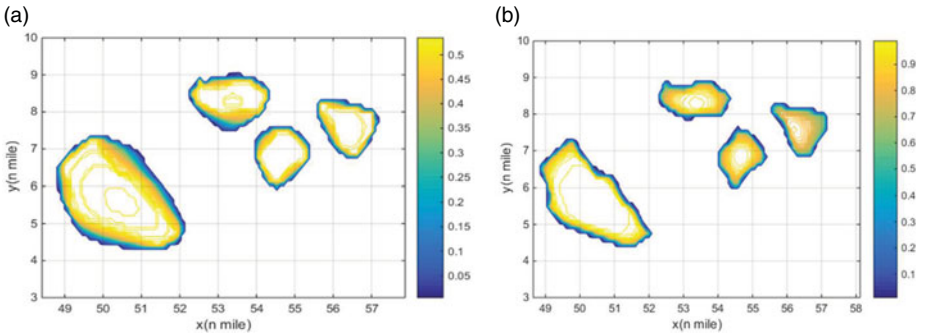

Figure 14. *Potential field of 20 · 0 m depth area: (a)* $\alpha = 5 \cdot 0$*, (b)* $\alpha = 50 \cdot 0$*.*

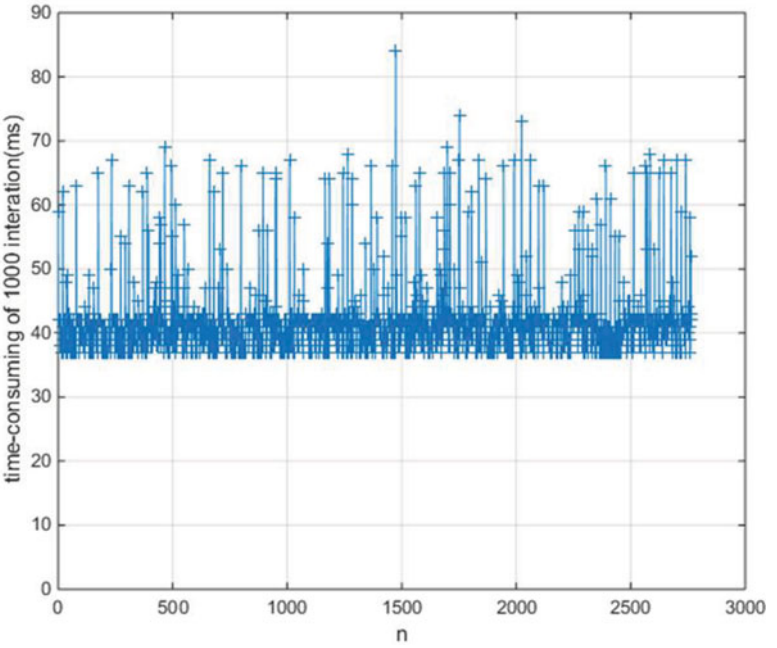

Figure 15. *Time consumption of 1,000 iterations in calculating the EPF for each point.*

angle. At 25 min, *KangHe* started to carry out OA actions to the second and third islands in succession, and the speed of the ship decreased correspondingly owing to the frequent course alteration. At 46 min, *KangHe* passed and cleared all the islands and altered its course to head for the final destination.

5.4. Path planning in restricted water and with multiple TSs ($\alpha = 50 \cdot 0$*)*

This section presents how the container ship *KangHe* (OS) was used as a smart ship along with two target container ships, *YinHe* (TS1) and *AnGuangJiang* (TS2), to complete the collaborative CA and OA experiment. The initial conditions and ship particulars are presented in Figure 19(a) and Table 3. $\alpha = 50 \cdot 0$ was set for the 20 · 0 m isobath data, and the CA parameters are listed in Table 4.

Figure 19(b) shows the collaborative CA and OA results obtained by *KangHe*. Figures 20 and 21 show the speed and course changing processes, respectively, and Figure 22 shows the DCPAs, TCPAs, and distances during the entire test. By analysing the results and intermediate processes, we observed that the ship navigated on the route plan at full speed in the first 5 min because there was no risk of

https://doi.org/10.1017/S0373463322000455 Published online by Cambridge University Press

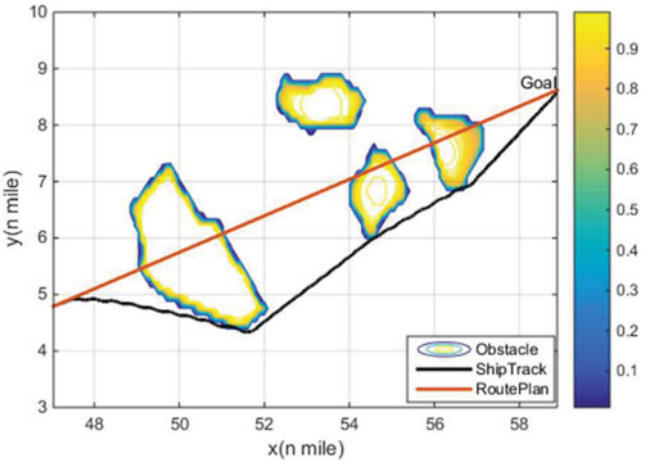

Figure 16. *OA result for KangHe ($\alpha = 50 \cdot 0$).*

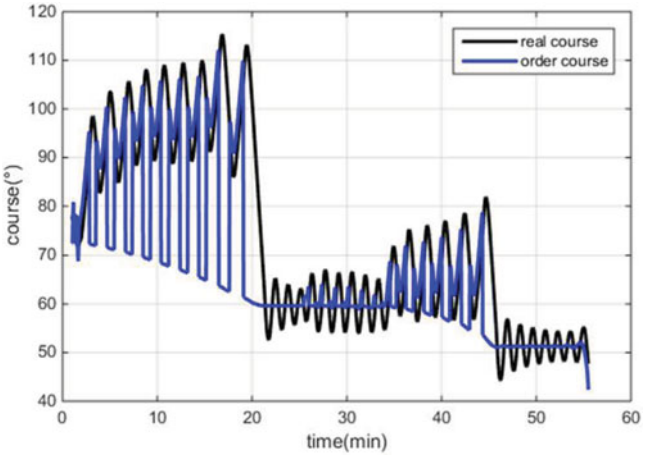

Figure 17. *Course of KangHe in OA test.*

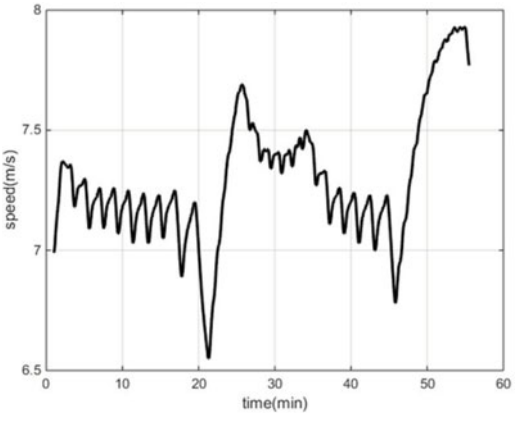

Figure 18. *Speed of KangHe in OA test.*

https://doi.org/10.1017/S0373463322000455 Published online by Cambridge University Press

Table 2. *Particulars and the initial condition of KangHe.*

Name	Length (m)	Breadth (m)	Draft (m)	Disp. (m^3)	Speed (kn)	Course (°)	Initial position	Goal's position
KangHe	259 · 0	32 · 0	9 · 5	43,067.0	16 · 0	358 · 6	39 · 0125732° 122 · 660690°	39 · 074040° 122 · 911545°

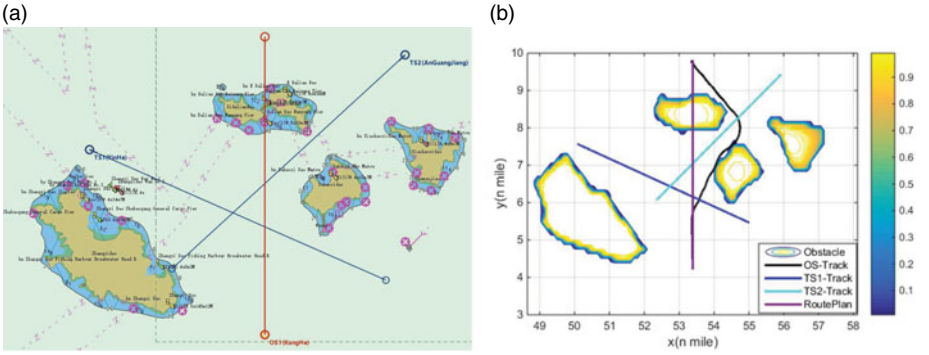

Figure 19. *Initial conditions of the scenario and collaborative CA results for KangHe: (a) initial scenario conditions, (b) collaborative CA and OA results.*

Table 3. *Particulars and initial conditions of ships.*

	Name	Length (m)	Breadth (m)	Draft (m)	Disp. (m^3)	Speed (kn)	Course (°)	Initial position	Goal's position
OS	*KangHe*	259 · 0	32 · 0	9 · 5	43,067.0	16 · 0	358 · 6	39 · 002470° 122 · 794723°	39 · 097142° 122 · 794723°
TS1	*YinHe*	168 · 0	28 · 0	9 · 5	28,849.0	12 · 0	113 · 1	39 · 061300° 122 · 722850°	39 · 019707° 122 · 844125°
TS2	*AnGuangJiang*	147 · 0	22 · 0	9 · 0	19,708.0	11 · 0	226 · 7	39 · 091487° 122 · 852053°	39 · 023353° 122 · 756428°

Table 4. *Parameters for CA tests.*

Item	Value	Item	Value
Emergency CA range criterion	$d_{emg} = 1 \cdot 0$ nm	Negotiation CA range criterion	$d_{neg} = 3 \cdot 0$ nm
Emergency CA DCPA-TCPA criterion	$tTOL_{emg\text{ - }CPA} = 6 \cdot 0$ min $dTOL_{emg\text{ - }CPA} = 1 \cdot 0$ nm	Negotiation CA DCPA-TCPA criterion	$tTOL_{neg\text{ - }CPA} = 12 \cdot 0$ min $dTOL_{neg\text{ - }CPA} = 2 \cdot 0$ nm
Obstacle detection range on OS course direction	OSSpeed*9 · 0 min	Limitation to course alteration	4 · 0°/3 s

https://doi.org/10.1017/S0373463322000455 Published online by Cambridge University Press

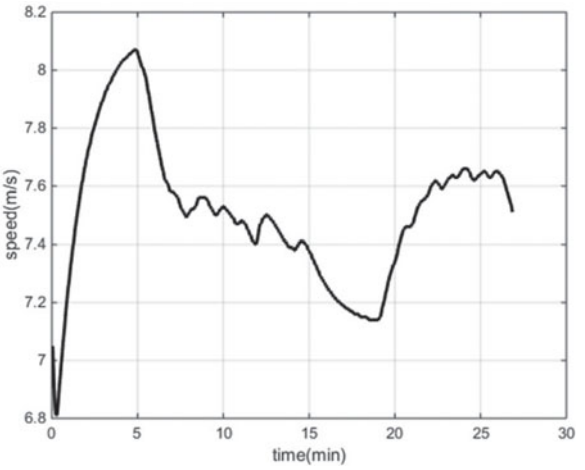

Figure 20. *Speed of KangHe.*

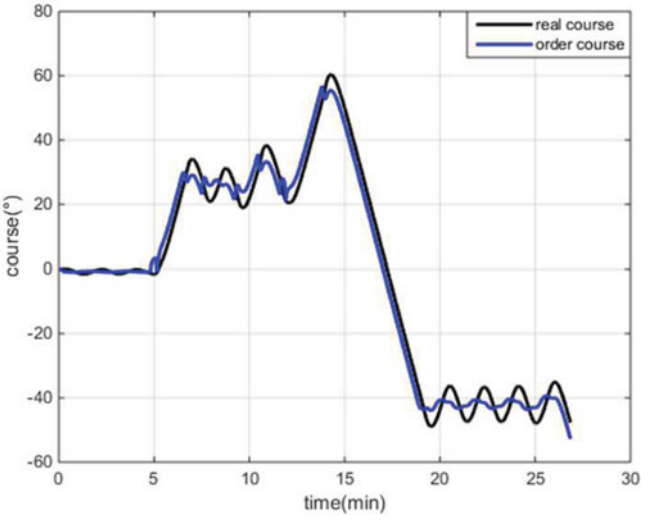

Figure 21. *Course of KangHe.*

collision between OS and TSs or obstacles. With the distances between OS and TSs decreasing, the DCPAs and TCPAs decreased accordingly; at 5 min, *KangHe* started to alter course to starboard as the CA criteria (Negotiation CA TCPA-DCPA and range criterion) with TS1 was fulfilled. At 7 min, the CA criteria with TS2 was fulfilled, *KangHe* started to carry out CA action with TS1 and TS2, and take OA actions around the islands simultaneously. At 14 min, *KangHe* started to head for the final destination when it had passed and cleared both TSs and obstacles.

According to the criteria in Table 4, *KangHe* should maintain a desired DCPA from all vessels and keep a safe distance of $2 \cdot 0$ nm from them. Owing to the restriction of obstacles provided by electronic chart, even though the largest CA actions were applied, *KangHe* passed and cleared at a distance of $1 \cdot 81$ nm from TS1 and a distance of $0 \cdot 38$ nm from TS2, respectively.

https://doi.org/10.1017/S0373463322000455 Published online by Cambridge University Press

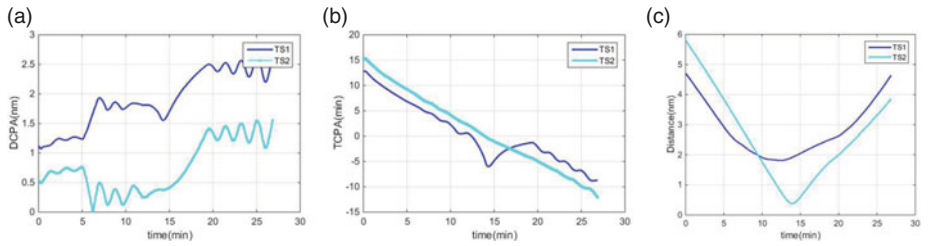

Figure 22. *DCPAs, TCPAs, and distances between KangHe and TSs: (a) DCPAs, (b) TCPAs, (c) distances.*

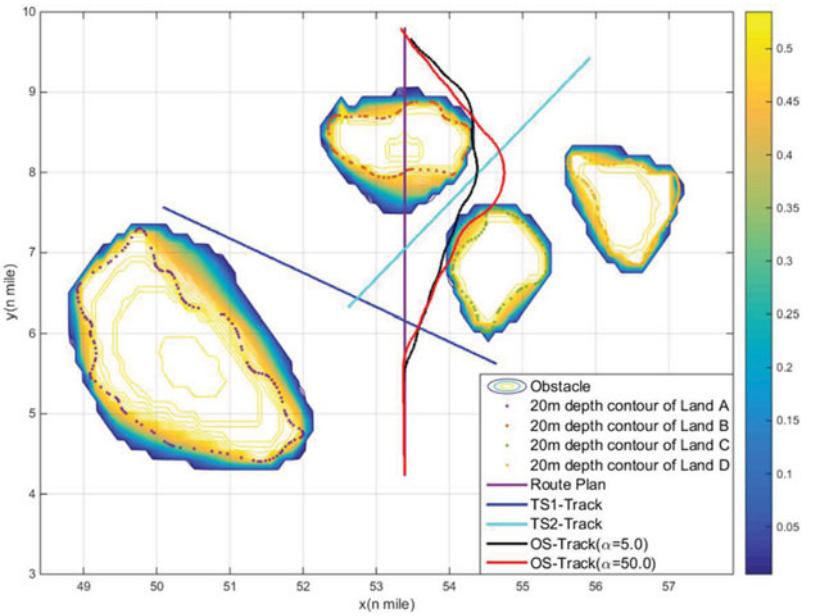

Figure 23. *Collaborative CA and OA results for KangHe.*

5.5. Path planning in restricted water and with multiple TSs ($\alpha = 5 \cdot 0$)

We set $\alpha = 5 \cdot 0$ for the $20 \cdot 0$ m isobath data to decrease the navigable area around the islands and conducted the same collaborative CA and OA experiment shown in Section 5.4. Figure 23 shows the CA results for *KangHe*. Comparisons with the results in Section 5.4 are shown in Figures 23–26. The results show that, in both experiments, the ship conducted the largest CA actions to maintain a relatively safe range of distance from obstacles and other ships.

Through comparison with the results in Section 5.4 (as shown in Figure 26), it can be observed that a smaller value of α induces a larger effective range around the obstacles while reducing the safe navigable region of the ship and restricting the scope of actions. In both experiments, *KangHe* started to carry out CA action with TS1 at 5 min, and then took CA action with TS1 and TS2 simultaneously. For the restriction of obstacles provided by the electronic chart, *KangHe* could not pass and clear the TSs at the desired safe distance of $2 \cdot 0$ nm. Because the effective range of the obstacles is larger than that in Section 5.4, the ship needs greater actions to maintain a larger distance from the islands while the action scope in relation to the other ships decreased. Finally, as listed in Table 5, *KangHe* passed and cleared TS1 and TS2 at distances of $1 \cdot 72$ nm and $0 \cdot 16$ nm, respectively; these distances are smaller than those in Section 5.4.

https://doi.org/10.1017/S0373463322000455 Published online by Cambridge University Press

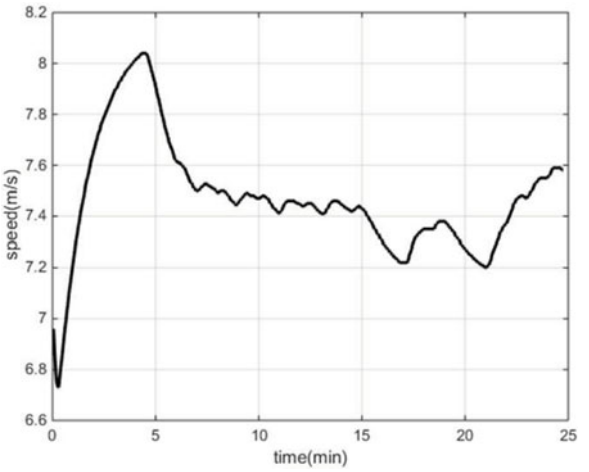

Figure 24. *Speed of KangHe.*

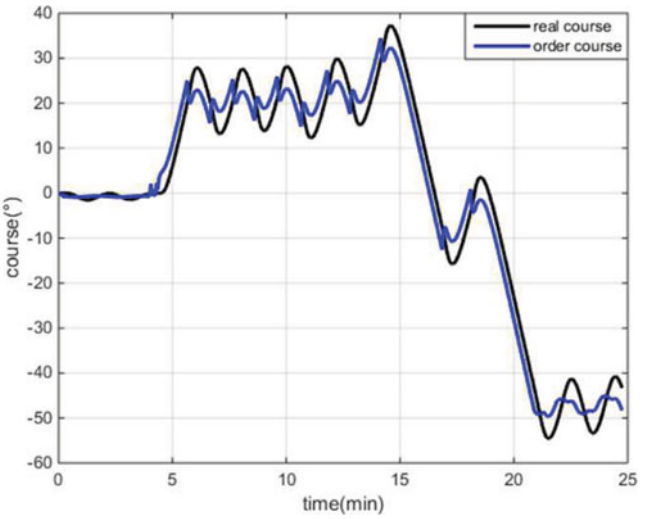

Figure 25. *Course of KangHe.*

6. Discussion

From the standpoint of engineering application, this paper proposes a novel environmental potential field modelling method based on *R*-function theory and within the ECDIS framework, and solves the awkward EPF modelling problems in APF-based path planning. The contributions of this study can be summarised as follows:

(1) An accurate EPF model is established based on ENC data to describe different types of obstacles, navigable areas, and non-navigable areas.
(2) A highly efficient and automatic EPF modelling method for complicated face objects is proposed based on *R*-function theory and discrete-convex hull technology.
(3) This study combines the accurate face object EPF model and improved APF method to realise the collaborative CA and OA.
(4) The system was developed in C++ and within the ECDIS framework. Collaborative CA and OA experiments were designed and conducted in a simulated environment to verify the effectiveness of the proposed EPF modelling method.

https://doi.org/10.1017/S0373463322000455 Published online by Cambridge University Press

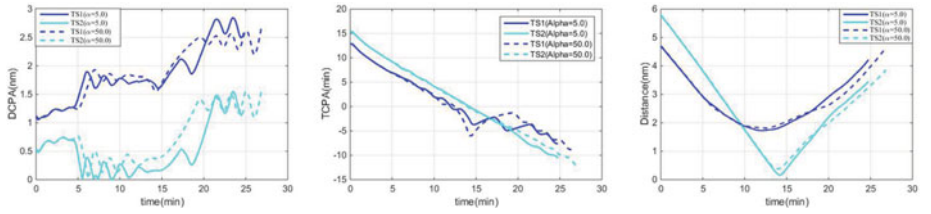

Figure 26. *DCPAs, TCPAs, and distances between KangHe and TSs: (a) DCPAs, (b) TCPAs, (c) distances.*

Table 5. *CA results for KangHe.*

Item	$\alpha = 50 \cdot 0$	$\alpha = 5 \cdot 0$
Maximum course alteration	$60 \cdot 4°$	$37 \cdot 2°$
Pass and clear distance from TS1	$1 \cdot 82$ nm	$1 \cdot 72$ nm
Pass and clear distance from TS2	$0 \cdot 38$ nm	$0 \cdot 16$ nm
Head for destination course	317°	311°

The proposed EPF modelling approach and path planning method were systematically tested (see Section 5). The results show that:

(1) The hierarchical structures of any complicated face object can be obtained automatically using the discrete-convex hull method, regardless of their concave-convex structures.
(2) The proposed EPF modelling method is accurate, because the data are provided by the officially released ENC data, and the *R*-function representation for face objects in the 2D plane is accurate.
(3) Through tests based on $20 \cdot 0$ m isobath data from Zhangzidao (Dalian, China), the proposed EPF modelling approach is proven to be accurate and reliable. As the proposed EPF modelling approach has very small calculations, it can be used in MASS real-time path planning.
(4) The collaborative CA and OA results show that the combination of the improved APF and EPF models is effective for MASS path planning, and different CA results can be obtained by setting different CA parameters for the ENC data.

For the future work, our research will be continued and improved in several ways. First, the EPF of an entire harbour will be established based on ENC data (tens of thousands of sampling points including lands, islands, navigation aids, isolated point objects, channel, etc.). Second, the current algorithm is mainly in accordance with rules 8 and 13–17 of COLREGS, and the OS acts as a give-way vessel; it is necessary to improve it to obey more rules. Third, the COLREGS-constrained APF model and EPF modelling method require more real-life tests to ensure their completeness. Fourth, we expect an early real-ship test of the proposed approach as an auxiliary CA system.

7. Conclusions

This study systematically solves the EPF modelling problems of complex geometric objects. In this study, reliable environmental data were provided by the officially released ENC data. The proposed EPF modelling method based on the *R*-function theory in this study can establish the potential field of any complex face object even if the object embodies a very complex concave-convex structure. The modelling procedure is simple and easy to conduct, offline extraction or mesh dividing operation of the ENC data is unnecessary, and the EPF modelling can be realised automatically without any manual intervention within the framework of the ECDIS. The proposed method is important for engineering applications of intelligent CA systems and is also a feasible path planning method for inland river ships.

https://doi.org/10.1017/S0373463322000455 Published online by Cambridge University Press

Acknowledgements. This research was partially supported by: the National Natural Science Foundation of China (No. 52071049); the project 'Intelligent Ship Testing and Verification' (No. 2018/473); the Natural Science Foundation Guidance Project of Liaoning Province (No. 2019-ZD-0152); and the project 'Maneuvering Simulation of Yunnan Inland Shipping Ships' (No. 851333).

Data availability. The data used to support the findings of this study are available from the corresponding author upon request.

References

Brcko, T., Androjna, A., Srše, J. and Boć, R. (2021). Vessel multi-parametric collision avoidance decision model: fuzzy approach. *Journal of Marine Science and Engineering*, **9**(1), 1–24. doi:10.3390/jmse9010049

Chen, P., Huang, Y., Mou, J. and van Gelder, P. H. A. J. M. (2018). Ship collision candidate detection method: a velocity obstacle approach. *Ocean Engineering*, **170**, 186–198. doi:10.1016/j.oceaneng.2018.10.023

Cheng-Bo, W., Xin-Yu, Z., Jia-Wei, Z., Zhi-Guo, D. and Lan-Xuan, A. N. (2019). Navigation behavioural decision-making of MASS based on deep reinforcement learning and artificial potential field. *Journal of Physics: Conference Series*, **1357**(1). doi:10.1088/1742-6596/1357/1/012026

Cheng, Y. and Zhang, W. (2018). Concise deep reinforcement learning obstacle avoidance for underactuated unmanned marine vessels. *Neurocomputing*, **272**, 63–73. doi:10.1016/j.neucom.2017.06.066

Chiang, H. T., Malone, N., Lesser, K., Oishi, M. and Tapia, L. (2015). Path-Guided Artificial Potential Fields with Stochastic Reachable Sets for Motion Planning in Highly Dynamic Environments. *Proceedings - IEEE International Conference on Robotics and Automation*, **2015**, 2347–2354. doi:10.1109/ICRA.2015.7139511

Dobkin, D., Guibas, L., Hershberger, J. and Snoeyink, J. (1993). An efficient algorithm for finding the CSG representation of a simple polygon. *Algorithmica*, **10**(1), 1–23. doi:10.1145/54852.378472

Du, L., Banda, O. A. V., Huang, Y., Goerlandt, F., Kujala, P. and Zhang, W. (2021). An empirical ship domain based on evasive maneuver and perceived collision risk. *Reliability Engineering and System Safety*, **213**. https://doi.org/10.1016/j.ress.2021.107752

Eriksen, B. O. H., Wilthil, E. F., Flåten, A. L., Brekke, E. F. and Breivik, M. (2018). Radar-Based Maritime Collision Avoidance Using Dynamic Window. *IEEE Aerospace Conference Proceedings*, 1–9 March 2018. doi:10.1109/AERO.2018.8396666

Fan, X., Guo, Y., Liu, H., Wei, B. and Lyu, W. (2020). Improved artificial potential field method applied for AUV path planning. *Mathematical Problems in Engineering*, **2020**. doi:10.1155/2020/6523158

Fiskin, R., Nasiboglu, E. and Yardimci, M. O. (2020). A knowledge-based framework for two-dimensional (2D) asymmetrical polygonal ship domain. *Ocean Engineering*, **202**. doi:10.1016/j.oceaneng.2020.107187

Fougerolle, Y. D., Gribok, A., Foufou, S., Truchetet, F. and Abidi, M. A. (2005). Boolean operations with implicit and parametric representation of primitives using R-functions. *IEEE Transactions on Visualization and Computer Graphics*, **11**(5), 529–538. doi:10.1109/TVCG.2005.72

Gan, J., Yuan, H., Li, S., Peng, Q. and Zhang, H. (2021). An analytical method for shallow spherical shell free vibration on two-parameter foundation. *Heliyon*, **7**, 1. doi:10.1016/j.heliyon.2020.e05876

Huang, Y., Chen, L., Chen, P., Negenborn, R. R. and van Gelder, P. H. A. J. M. (2020). Ship collision avoidance methods: State-of-the-art. *Safety Science*, **121**, 451–473. doi:10.1016/j.ssci.2019.09.018

Kuwata, Y., Wolf, M. T., Zarzhitsky, D. and Huntsberger, T. L. (2014). Safe maritime autonomous navigation with COLREGS, using velocity obstacles. *IEEE Journal of Oceanic Engineering*, **39**(1), 110–119. https://doi.org/ 10.1109/JOE.2013.2254214

Li, L., Wu, D., Huang, Y. and Yuan, Z. M. (2021). A path planning strategy unified with a COLREGS collision avoidance function based on deep reinforcement learning and artificial potential field. *Applied Ocean Research*, **113**. doi:10.1016/j.apor.2021.102759

Liu, J.-Y. and Ahang, H.-L. (2001). An introduction to theory of R-functions and a survey on their applications. *Journal of Engineering Graphics*, **02**, 114–123.

Liu, Y. and Bucknall, R. (2015). Path planning algorithm for unmanned surface vehicle formations in a practical maritime environment. *Ocean Engineering*, **97**, 126–144. doi:10.1016/j.oceaneng.2015.01.008

Liu, Y. and Bucknall, R. (2018). Efficient multi-task allocation and path planning for unmanned surface vehicle in support of ocean operations. *Neurocomputing*, **275**, 1550–1566. doi:10.1016/j.neucom.2017.09.088

Lu, Z. R. and Wang, L. (2019). Cavity identification in elastic structures by explicit domain mapping and boundary mode sensitivity analysis. *European Journal of Mechanics, A/Solids*, **75**, 109–127. doi:10.1016/j.euromechsol.2019.01.015

Lyu, H. and Yin, Y. (2018a). Fast path planning for autonomous ships in restricted waters. *Applied Sciences (Switzerland)*, **8**(12). doi:10.3390/app8122592

Lyu, H. and Yin, Y. (2018b). Ship's Trajectory Planning for Collision Avoidance at Sea Based on Modified Artificial Potential Field. *2nd International Conference on Robotics and Automation Engineering, ICRAE 2017*, 2017, 351–357. doi:10.1109/ICRAE.2017.8291409

Lyu, H. and Yin, Y. (2019a). Path planning of autonomous ship based on electronic chart vector data modelling. *Journal of Transport Information and Safety*, **37**(5), 94–106.

Lyu, H. and Yin, Y. (2019b). COLREGS-constrained real-time path planning for autonomous ships using modified artificial potential fields. *Journal of Navigation*, **72**(3), 588–608. doi:10.1017/S0373463318000796

Montiel, O., Orozco-Rosas, U. and Sepúlveda, R. (2015). Path planning for mobile robots using bacterial potential field for avoiding static and dynamic obstacles. *Expert Systems with Applications*, **42**(12), 5177–5191. doi:10.1016/j.eswa.2015.02.033

Mousazadeh, H., Jafarbiglu, H., Abdolmaleki, H., Omrani, E., Monhaseri, F., Abdollahzadeh, M. R., Mohammadi-Aghdam, A., Kiapei, A., Salmani-Zakaria, Y. and Makhsoos, A. (2018). Developing a navigation, guidance and obstacle avoidance algorithm for an unmanned surface vehicle (USV) by algorithms fusion. *Ocean Engineering*, **159**, 56–65. doi:10.1016/j.oceaneng.2018.04.018

Öztürk, Ü, Akdağ, M. and Ayabakan, T. (2022). A review of path planning algorithms in maritime autonomous surface ships: Navigation safety perspective. *Ocean Engineering*, **251**, 111010. doi:10.1016/j.oceaneng.2022.111010

Panda, M., Das, B., Subudhi, B. and Pati, B. B. (2020). A comprehensive review of path planning algorithms for autonomous underwater vehicles. *International Journal of Automation and Computing*, **17**(3), 321–352. doi:10.1007/s11633-019-1204-9

Peng, Y., Huang, Z., Tan, J. and Liu, Y. (2016). Calculating minimum distance between geometric objects represented with R-functions. *Mechanical Science and Technology for Aerospace Engineering*, **35**(9), 1330–1336.

Pêtrès, C., Romero-Ramirez, M. A. and Plumet, F. (2012). A potential field approach for reactive navigation of autonomous sailboats. *Robotics and Autonomous Systems*, **60**(12), 1520–1527. doi:10.1016/j.robot.2012.08.004

Rawson, A. and Brito, M. (2021). A critique of the use of domain analysis for spatial collision risk assessment. *Ocean Engineering*, **219**, doi:10.1016/j.oceaneng.2020.108259

Ren, J., McIsaac, K. A., Patel, R. V. and Peters, T. M. (2007). A potential field model using generalized sigmoid functions. *IEEE Transactions on Systems, Man, and Cybernetics, Part B: Cybernetics*, **37**(2), 477–484. doi:10.1109/TSMCB.2006.883866

Rvachev, V. L. (1982). Theory of R-functions and some applications. *Econometrica*, **36**(5), 35–38.

Sang, H., You, Y., Sun, X., Zhou, Y. and Liu, F. (2021). The hybrid path planning algorithm based on improved A* and artificial potential field for unmanned surface vehicle formations. *Ocean Engineering*, **223**. doi:10.1016/j.oceaneng.2021.108709

Serigstad, E., Eriksen, B.-O. H. and Breivik, M. (2018). *Hybrid collision avoidance for autonomous surface vehicles, IFAC PapersOnLine*, 51-29, 1–7. doi:10.1016/j.ifacol.2018.09.460

Shaobo, W., Yingjun, Z. and Lianbo, L. (2020). A collision avoidance decision-making system for autonomous ship based on modified velocity obstacle method. *Ocean Engineering*, **215**, 107910. doi:10.1016/j.oceaneng.2020.107910

Shi, C., Zhang, M. and Peng, J. (2007). Harmonic Potential Field Method for Autonomous Ship Navigation. *Proceedings, 7th International Conference on Intelligent Transport Systems Telecommunications*, 471–476. doi:10.1109/ITST.2007.4295916

Souissi, O., Benatitallah, R., Duvivier, D., Artiba, A., Belanger, N. and Feyzeau, P. (2013). Path Planning: a 2013 Survey. *Proceedings of 2013 International Conference on Industrial Engineering and Systems Management, IEEE - IESM 2013*, 809–816. https://ieeexplore.ieee.org/document/6761521

Sukumar, N. and Srivastava, A. (2022). Exact imposition of boundary conditions with distance functions in physics-informed deep neural networks. *Computer Methods in Applied Mechanics and Engineering*, **389**, 114333. doi:10.1016/j.cma.2021.114333

Tam, C. K., Bucknall, R. and Greig, A. (2009). Review of collision avoidance and path planning methods for ships in close range encounters. *Journal of Navigation*, **62**(3), 455–476. doi:10.1017/S0373463308005134

Tao, S. and Tan, J. (2018). Path planning with obstacle avoidance based on normalized R-functions. *Journal of Robotics*, **2018**, 1–10. doi:10.1155/2018/5868915

Vagale, A., Bye, R. T., Oucheikh, R., Osen, O. L. and Fossen, T. I. (2021a). Path planning and collision avoidance for autonomous surface vehicles I: A review. *Journal of Marine Science and Technology (Japan)*, **26**(4), 1292–1306. doi:10.1007/s00773-020-00790-x

Vagale, A., Bye, R. T., Oucheikh, R., Osen, O. L. and Fossen, T. I. (2021b). Path planning and collision avoidance for autonomous surface vehicles II: A comparative study of algorithms. *Journal of Marine Science and Technology (Japan)*, **26**(4), 1307–1323. doi:10.1007/s00773-020-00790-x

Varvak, M. (2015). Ellipsoidal/radial basis functions neural networks enhanced with the Rvachev function method in application problems. *Engineering Applications of Artificial Intelligence*, **38**, 111–121. doi:10.1016/j.engappai.2014.09.017

Wang, N., Gao, Y., Zheng, Z., Zhao, H. and Yin, J. (2018). A Hybrid Path-Planning Scheme for an Unmanned Surface Vehicle. *8th International Conference on Information Science and Technology, ICIST 2018*, 231–236. doi:10.1109/ICIST.2018.8426161

Wang, S. M., Fang, M. C. and Hwang, C. N. (2019). Vertical obstacle avoidance and navigation of autonomous underwater vehicles with H∞ controller and the artificial potential field method. *Journal of Navigation*, **72**(1), 207–228. doi:10.1017/S0373463318000589

Wu, J., Wang, X., Jiang, H., Zheng, K. and R. L. (2003). Representation for polygons with implicit function. *Computer Engineering and Applications*, **32**, 87–89.

Xue, Y., Clelland, D., Lee, B. S. and Han, D. (2011). Automatic simulation of ship navigation. *Ocean Engineering*, **38**(17–18), 2290–2305. doi:10.1016/j.oceaneng.2011.10.011

Yuan, X., Zhang, D., Zhang, J., Zhang, M. and Guedes Soares, C. (2021). A novel real-time collision risk awareness method based on velocity obstacle considering uncertainties in ship dynamics. *Ocean Engineering*, **220**. doi:10.1016/j.oceaneng.2020.108436

Zhang, X., Wang, C., Jiang, L., An, L. and Yang, R. (2021). Collision-avoidance navigation systems for maritime autonomous surface ships: A state of the art survey. *Ocean Engineering*, **235**. doi:10.1016/j.oceaneng.2021.109380

Cite this article: Zhu Z, Lyu H, Zhang J, Yin Y, Fan X (2023). A practical environment potential field modelling method for complex geometric objects. *The Journal of Navigation* **76**: 1, 38–61. https://doi.org/10.1017/S0373463322000455